Adaptive Single-end Protection for DC Grid with Dedicated Metallic Return Based on Transient Mean Value of Current Limiting Reactor Modal Voltage

Yuhong Wang, *Senior Member*, *IEEE*, Zipeng Tan, Jianquan Liao, *Member*, *IEEE*, Yangtao Liu, Chunsheng Guo, *Student Member*, *IEEE*, Niancheng Zhou, *Senior Member*, *IEEE*, and Qianggang Wang, *Senior Member*, *IEEE*

***Abstract*—In a DC grid with dedicated metallic return (DMR), the coupling effects among the positive pole, negative pole, and DMR conductors must be considered, which makes fault identification particularly difficult. In addition, the identification of high-impedance faults remains a major challenge for DC grid protection. To address these issues, this study proposes an adaptive single-end protection method for DC grid based on the transient mean value of the current limiting reactor (CLR) modal voltage. First, a fault analysis model of the DC grid with DMR is established using the Clarke transformation. The characteristics of CLR modal voltage are then clarified. A fault pole-selection method based on a novel modulus phase plane is next proposed. A threshold scaling factor based on the differential of DC bus voltage is then constructed to enhance the sensitivity and rapidity of the protection, which can adaptively modify the threshold according to the fault severity. Finally, a simulation model of a four-terminal DC grid with DMR is developed in PSCAD/EMTDC. The speed and reliability of the proposed protection method are verified by simulations and experiments.**

***Index Terms*—Clarke transformation, modulus decomposition, DC grid, dedicated metallic return (DMR), DC grid protection, single-end protection, scaling factor, current limiting reactor (CLR).**

I. Introduction

With the rapid growth of renewable energy generation, the modular multilevel converter (MMC) based DC grids play an increasingly critical role in high-voltage and large-capacity power transmission scenarios [1], [2]. In recent years, an increasing number of DC transmission projects based on overhead lines (OHLs) have been implemented [3]-[5], which pose significant challenges to DC grids. On the one hand, the complex operating conditions of OHLs greatly increase the probability of line faults. On the other hand, a rapid increase in the fault currents significantly shortens the timescale of fault identification. In addition, the existing protection algorithms are inadequate with regard to the accuracy of identifying high-impedance faults (HIFs) [6].

Previous studies have categorized protections for DC grid lines into two types: single-end protection and pilot protection [7], [8]. Single-end protection is preferred as a primary protection due to its shorter response time and reduced communication delays [9]. Existing single-end protections can be based on the following four technologies: travelling wave, artificial intelligence (AI), parameter identification, and electrical transformation.

Using travelling wave signals for fault identification is an effective method for multi-terminal flexible DC systems, as demonstrated in [10]. However, this method can be easily affected by measurement noises from sensors. In addition, the protection methods based on traditional travelling wave may fail due to transient fault resistance [11]. The wavelet transform based time-frequency analysis algorithms are introduced in [12] and [13] to enhance the protection reliability.

With the rapid development of AI technology, the protection methods based on AI have become available. These methods utilize neural networks that incorporate transient fault resistances and noises into the training process, thus improving the protection accuracy [14], [15].

Researchers have also investigated protection methods based on parameter identification. In [16], a fault model for a single-conductor transmission line is constructed that uses actual and estimated values to detect faults [16]. This model

Manuscript received: February 5, 2024; revised: June 3, 2024; accepted: August 5, 2024. Date of CrossCheck: August 5, 2024. Date of online publication: September 19, 2024.

This work was supported in part by the Joint Funds of the National Natural Science Foundation of China (No. U22B6006), the National Natural Science Foundation of China (No. 52207126), and Natural Science Foundation of Sichuan Province (No. 2023NSFSC0296).

Y. Wang, Z. Tan, J. Liao (corresponding author), Y. Liu, and C. Guo are with the College of Electrical Engineering, Sichuan University, Chengdu, China (e-mail: yuhongwang@scu.edu.cn; 2022223035199@stu.scu.edu.cn; jquanliao@scu.edu.cn; liuyangtao@stu.scu.edu.cn; kiritodile@outlook.com).

N. Zhou and Q. Wang are with the State Key Laboratory of Power Transmission Equipment Technology, School of Electrical Engineering, Chongqing University, Chongqing, China (e-mail: cee_nczhou@cqu. edu. cn; qianggang1987@cqu.edu.cn).

DOI: 10.35833/MPCE.2024.000138

has been extended to multipole transmission lines, thus broadening its application [17]. The aforementioned methods all require a significant amount of data and are limited to specific models, thus reducing their generalizability.

Several simple programs based on the average transient current are proposed in [18] and [19]. However, they are not sensitive to HIF. In [20] and [21], a protection method is developed based on the CLR voltage on the positive pole (PP) and negative pole (NP). Nevertheless, these methods lack robustness against fault impedance and neglect the coupling effect between poles, making them difficult to apply in engineering.

Considering the coupling in a grounded DC grid, [22] and [23] utilize the modulus decomposition to decouple the coupling relationships between the lines. In [22], a novel single-end protection scheme is adopted for DC grids that utilizes the derivatives of the common-mode (CM) and differential-mode (DM) currents of the protection phase plane. The CM and DM characteristics of the CLR voltage are analyzed for different fault types in [23] and [24], where a DC grid protection scheme that could discriminate between different fault types via analysis is proposed. Compared with the grounded DC grid, the DC grid with dedicated metallic return (DMR) can prevent metal corrosion and high currents flowing directly to the ground. However, this type of structure results in complex coupling relationships and fault types [25]. Protection methods for DC grid with DMR are proposed in [26] and [27], but it is challenging to distinguish between a pole-to-ground fault and a pole-to-DMR fault. Moreover, both protection methods in [26] and [27] are based on the travelling wave, which is primarily affected by the fault transition resistance.

To improve the accuracy and speed of protection for different fault types and to decouple the coupling relationship between lines in the DC grid with DMR, this study proposes an adaptive single-end protection method based on the transient mean value of CLR modal voltage. The contributions of this study are described as follows.

1) The equivalent modulus circuit of the DC grid with DMR is derived, which facilitates the characteristic analysis of CLR modal voltage, DC fault identification, and threshold settings. The CLR modal voltage expression specific to each fault type is obtained through mathematical analysis.

2) A novel single-end protection method is proposed, which uses a pole-selection phase plane composed of the transient mean values of 0-mode (0M) and 2-mode (2M) voltages. This method identifies different fault types in a DC grid and provides fast fault identification with robust reliability even when the fault circuit parameters vary significantly.

3) A threshold scaling factor is introduced, which adjusts the protection threshold according to fault severity. This adaptive method can enhance the recognition speed of critical faults and increase the sensitivity of HIF recognition.

The remainder of this paper is structured as follows. Section II presents comprehensive derivations of the MMC modulus circuits and fault transition resistance along with CLR modal voltage expressions for various fault types. Section III describes the protection procedure and adaptive method for the proposed protection method. Simulation and experimental results are presented in Section IV. Section V concludes this study.

II. Modulus Components of DC Grid

A. Equivalent Modulus Circuits of DC Grid Components

As shown in (1), the 1-mode (1M), 2M, and 0M components of the currents and voltages at the PP, NP, and DMR poles during a DC fault can be obtained using Clarke transformation. This finding is consistent with the results in [25].

$$\begin{bmatrix} y_1 \\ y_2 \\ y_0 \end{bmatrix} = \boldsymbol{A} \begin{bmatrix} y_p \\ y_m \\ y_n \end{bmatrix} = \frac{1}{6} \begin{bmatrix} 3 & 0 & -3 \\ 1 & -2 & 1 \\ 2 & 2 & 2 \end{bmatrix} \begin{bmatrix} y_p \\ y_m \\ y_n \end{bmatrix} \tag{1}$$

where y denotes the voltage or current; the subscripts 1, 0, and 2 indicate the 1M, 0M, and 2M components, respectively; $\boldsymbol{A}$ is the modulus transformation matrix; and the subscripts p, m, and n denote the PP component, DMR pole component, and NP component, respectively.

According to (1), y_1 flows only from the PP and returns from the NP, indicating the symmetric operating component of the system. By contrast, y_2 flows equally from the PP and NP and returns from the DMR, which indicates whether the system operates asymmetrically. In addition, y_0 has the same distribution in the PP, NP, and DMR, which indicates whether the system has a ground fault.

The structure of the DC grid with DMR is illustrated in Fig. 1 [26], [27]. MMC_4 is the grounding point of the system. In Fig. 1, p, m, and n denote the PP, DMR pole, and NP, respectively, which are symmetrically arranged; L_T is the inductance of CLR; f_1 and f_3 denote the backward external fault (BEF) and forward external fault (FEF) of the DC line, respectively; f_2 denotes the internal fault (IF) on the DC line; and x is the ratio to the total line length. In the case of a fault at f_4, $x=0\%$, whereas the fault at f_5 corresponds to $x=100\%$.

Based on the assumption that the MMC is not blocked in the event of a DC fault, it can be represented as an RLC series circuit [18]. The equivalent resistance and inductance of the MMC bridge arms are denoted as R_m and L_m, respectively. In addition, the equivalent resistance and inductance of MMC bridge arm after parallel connection satisfy $L_a=2L_m/3$ and $R_a=2R_m/3$, respectively.

Figure 2 shows the modulus circuit of MMC in the DC grid, where $Z_a(s)=R_a+\mathrm{j}X_a$ and $U_d(s)$ are the equivalent impedance and voltage of MMC, respectively; i_a and i_b are the input and output currents of MMC, respectively; U is the output voltage of MMC; and the subscripts 1, 0, 2, p, m, and n have the same meanings as those in (1).

The voltages and currents in Fig. 2 are expressed as:

$$\begin{cases} U_p(s)-U_m(s)=U_d(s)+Z_a(s)(i_{ap}(s)-i_{bp}(s)) \\ U_m(s)-U_n(s)=U_d(s)+Z_a(s)(i_{bn}(s)-i_{an}(s)) \\ i_{ap}(s)+i_{an}(s)+i_{am}(s)=i_{bp}(s)+i_{bn}(s)+i_{bm}(s) \end{cases} \tag{2}$$

Simplifying (2) with (1), the modal currents and voltages of MMC can be obtained as:

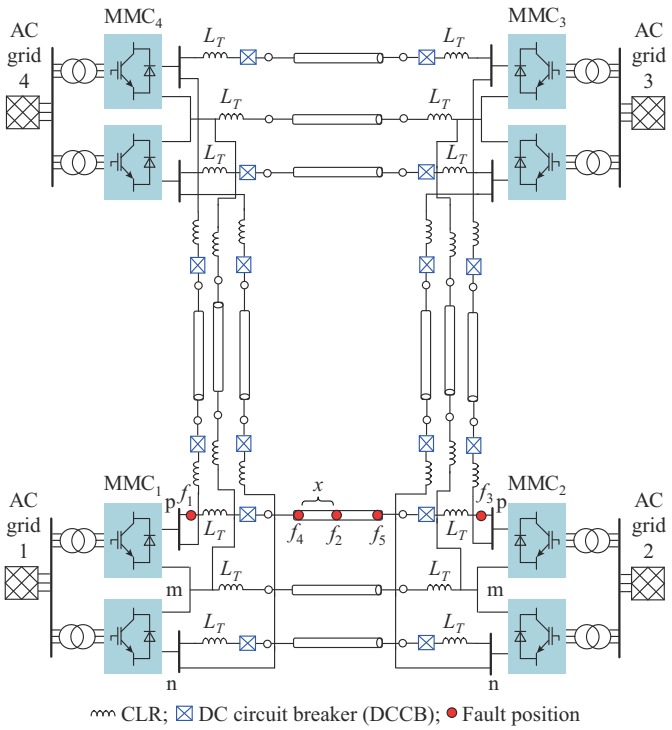

Fig. 1. Structure of DC grid with DMR.

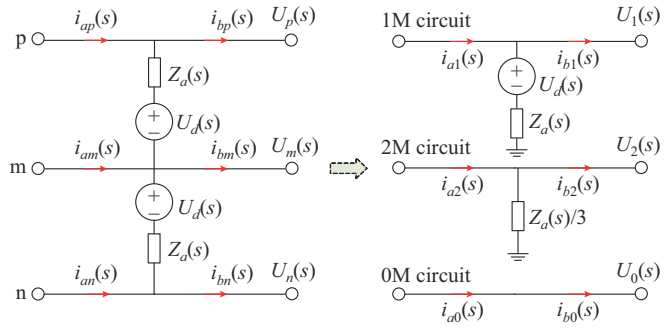

Fig. 2. Modulus circuit of MMC in DC grid.

$$\begin{cases} U_1(s)=U_d(s)+Z_a(s)(i_{a1}(s)-i_{b1}(s)) \\ U_2(s)=\dfrac{1}{3}Z_a(s)(i_{a2}(s)-i_{b2}(s)) \\ i_{a0}(s)=i_{b0}(s) \end{cases} \tag{3}$$

The DC line in the polar-component coordinate system can be transformed into the modal-component coordinate system using a modulus transformation matrix, as shown in (1). In the polar-component coordinate system, the mutual coupling exists among the PP, NP, and DMR poles. However, in the modal-component coordinate system, each modulus is independent of the others. The modal equivalent model of DC line is described in [25].

The fault types can be divided into pole-to-ground, pole-to-DMR, and pole-to-pole faults. Figure 3 shows the equivalent circuits under different fault types, where U_f and i_f are the fault voltage and current, respectively; and R_f is the fault transition resistance. As an example of various pole-to-pole faults, the PP-to-NP fault (PNF) is used for analysis. Besides, PGF, PMF, NGF, and NMF are short for the PP-to-ground fault, PP-to-DMR fault, NP-to-ground fault, and NP-to-DMR fault, respectively. As Fig. 3 illustrates, the fault currents and voltages satisfy different conditions under different fault types.

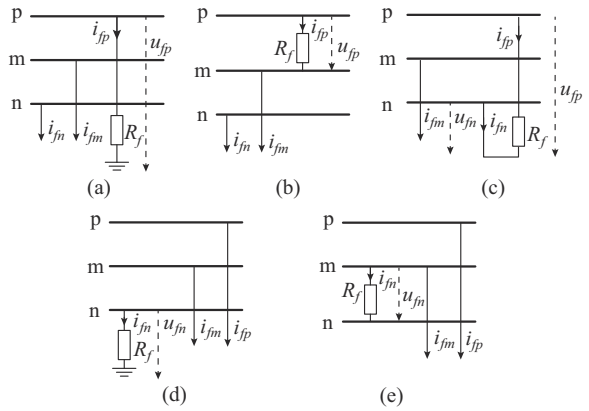

Fig. 3. Equivalent circuits under different fault types. (a) PGF. (b) PMF. (c) PNF. (d) NGF. (e) NMF.

The equivalent modulus circuit of fault transition resistance can be obtained by applying (1) to different fault types, as shown in Fig. 4.

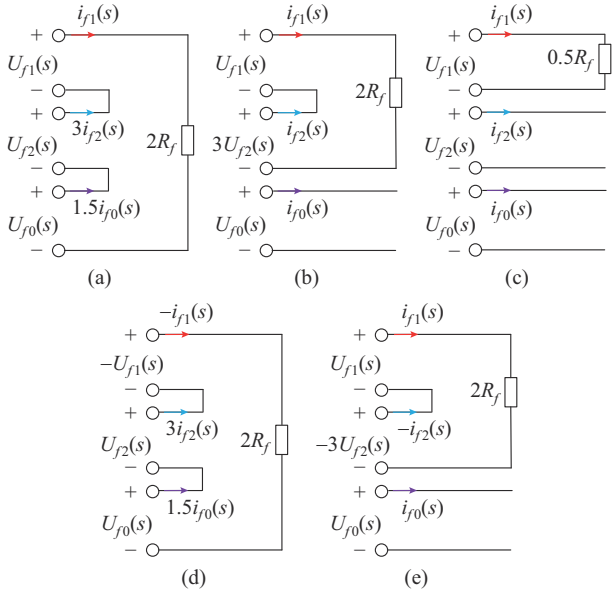

Fig. 4. Modulus circuit of fault transition resistance under different fault types. (a) PGF. (b) PMF. (c) PNF. (d) NGF. (e) NMF.

B. Composite Equivalent Modulus Circuits

Based on Fig. 1, this study presents composite equivalent modulus circuits for different IFs, which synthesizes the 1M, 2M, and 0M circuits as previously derived. Figure 5 shows the equivalent modulus circuits under PGF, PMF, and PNF, where $Z_{ak}=R_{ak}+\mathrm{j}X_{ak}$ is the impedance of MMC$_k$ ($k=1,2,3,4$); $Z_{i,j\text{-}k}=R_{i,j\text{-}k}+\mathrm{j}X_{i,j\text{-}k}$ is the total impedance of the line from MMC$_j$ to MMC$_k$ in the i-mode circuit ($i=0,1,2$, $j,k=1,2,3,4$, and $j\neq k$); $L_{T,j\text{-}k}$ is the inductance of CLR on the line from MMC$_j$ to MMC$_k$; and $U_{LT,i,j\text{-}k}$ is the i-mode voltage of CLR on the line from MMC$_j$ to MMC$_k$. As

NMF and NGF have structures similar to PMF and PGF, respectively, they are not depicted here.

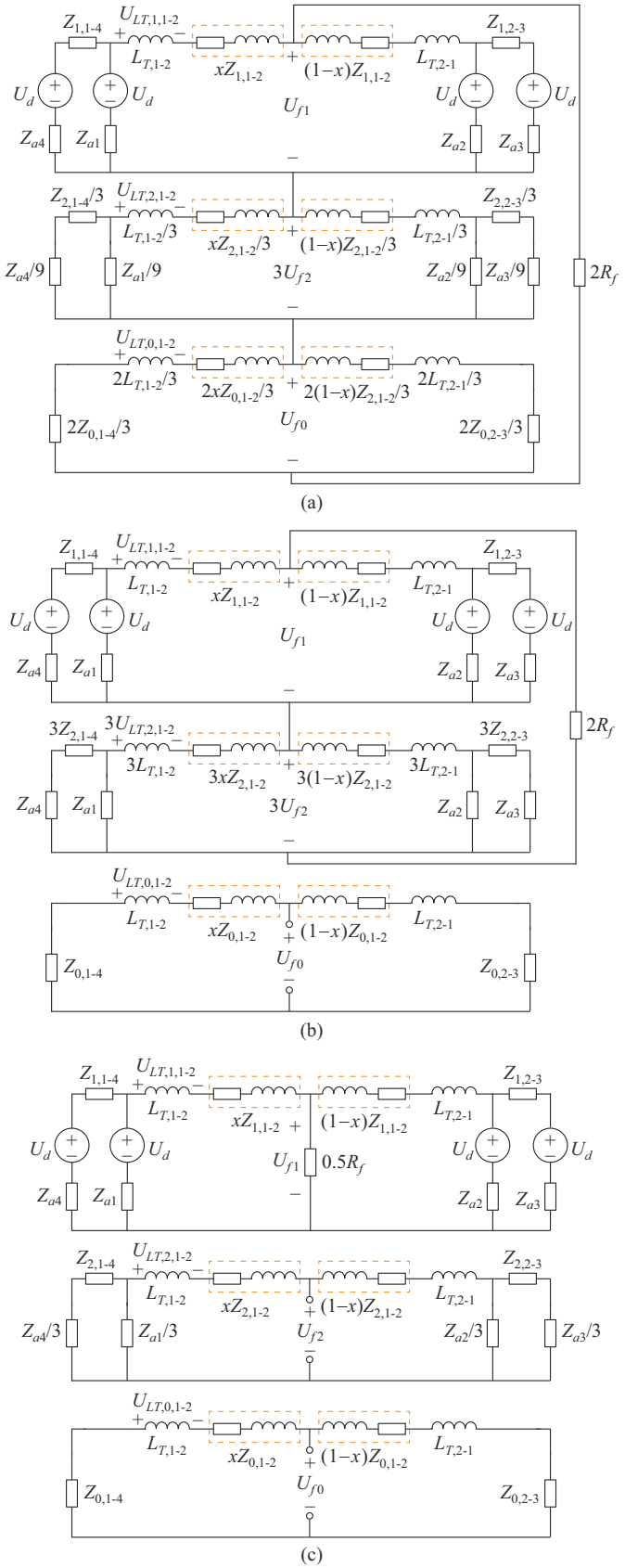

Fig. 5. Composite equivalent modulus circuits under different IFs. (a) PGF. (b) PMF. (c) PNF.

When an IF occurs on the line from MMC_1 to MMC_2, the 1M voltage of CLR $U_{LT,1,1-2}$ satisfies:

$$U_{LT,1,1-2}=\frac{sL_{T,1-2}U_d}{(Z_{a1}+Z_2+Z_{\Delta q}//Z_1)}-\frac{sL_{T,1-2}Z_{\Delta q}U_d}{(Z_{a2}+Z_4+Z_{\Delta q}//Z_3)(Z_{\Delta q}+Z_3)} \tag{4}$$

where $Z_{\Delta q}$ is the equivalent impedance for PGF, PMF, and PNF when $q=1,2,3$, respectively; and Z_1 - Z_4 and $Z_{\Delta q}(q=1,2,3)$ are the frequency-dependent functions that satisfy:

$$\begin{cases} Z_1=(1-x)Z_{1,1-2}+sL_{T,2-1}+Z_{a2} \\ Z_2=sL_{T,1-2}+xZ_{1,1-2} \\ Z_3=xZ_{1,1-2}+sL_{T,1-2}+Z_{a1} \\ Z_4=sL_{T,2-1}+(1-x)Z_{1,1-2} \end{cases} \tag{5}$$

$$\begin{cases} Z_{\Delta 1}=2R_f+\dfrac{2}{3}(Z_{01}//Z_{02})+\dfrac{1}{3}(Z_{21}//Z_{22}) \\ Z_{\Delta 2}=2R_f+3(Z_{21}//Z_{22}) \\ Z_{\Delta 3}=0.5R_f \end{cases} \tag{6}$$

$$\begin{cases} Z_{01}=xZ_{0,1-2}+Z_{0,1-4}+sL_{T,1-2} \\ Z_{02}=(1-x)Z_{0,1-2}+Z_{0,2-3}+sL_{T,2-1} \end{cases} \tag{7}$$

$$\begin{cases} Z_{21}=\dfrac{1}{3}Z_{a1}+sL_{T,1-2}+xZ_{2,1-2} \\ Z_{22}=\dfrac{1}{3}Z_{a2}+sL_{T,2-1}+(1-x)Z_{2,1-2} \end{cases} \tag{8}$$

In addition, when an IF occurs on the line from MMC_1 to MMC_2, the 2M and 0M voltages of CLR satisfy (9) and (10), respectively.

$$U_{LT,2,1-2}=\begin{cases} \dfrac{1}{3}\left[\dfrac{sL_{T,1-2}U_dZ_{22}Z_1}{(Z_{a1}+Z_2+Z_{\Delta q}//Z_1)(Z_{22}+Z_{21})(Z_{\Delta q}+Z_1)}+\dfrac{sL_{T,1-2}Z_3Z_{22}U_d}{(Z_{a2}+Z_4+Z_{\Delta q}//Z_3)(Z_{22}+Z_{21})(Z_{\Delta q}+Z_3)}\right] & \text{PGF} \\ \dfrac{sL_{T,1-2}U_dZ_{22}Z_1}{(Z_{a1}+Z_2+Z_{\Delta q}//Z_1)(Z_{22}+Z_{21})(Z_{\Delta q}+Z_1)}+\dfrac{sL_{T,1-2}Z_3Z_{22}U_d}{(Z_{a2}+Z_4+Z_{\Delta q}//Z_3)(Z_{22}+Z_{21})(Z_{\Delta q}+Z_3)} & \text{PMF} \\ 0 & \text{PNF} \end{cases} \tag{9}$$

$$U_{LT,0,1-2}=\begin{cases} \dfrac{2sL_{T,1-2}U_dZ_{02}Z_1}{3(Z_{a1}+Z_2+Z_{\Delta q}//Z_1)(Z_{02}+Z_{01})(Z_{\Delta q}+Z_1)}+\dfrac{2sL_{T,1-2}Z_3Z_{02}U_d}{3(Z_{a2}+Z_4+Z_{\Delta q}//Z_3)(Z_{02}+Z_{01})(Z_{\Delta q}+Z_3)} & \text{PGF} \\ 0 & \text{PMF or PNF} \end{cases} \tag{10}$$

Figures 4, 5(a), and 5(b) show that the amplitudes of the 2M and 0M voltages of CLR under an internal NGF are the same as those under an internal PGF but with opposite polarities. This also holds for the internal NMF. In this study, PGF is used as an illustrative example of IF.

Figures 5(a) and 6 show that the main difference between

the EFs and IF is the polarity of the CLR voltage and line inductance. Specifically, in the case of BEF, the 1M voltage of CLR has negative polarity. However, the 1M voltage of CLR assumes a positive polarity in the presence of an IF or FEF. Considering the boundary effect of CLR, the amplitude for the 1M voltage of CLR is higher when an IF occurs than that when an FEF occurs.

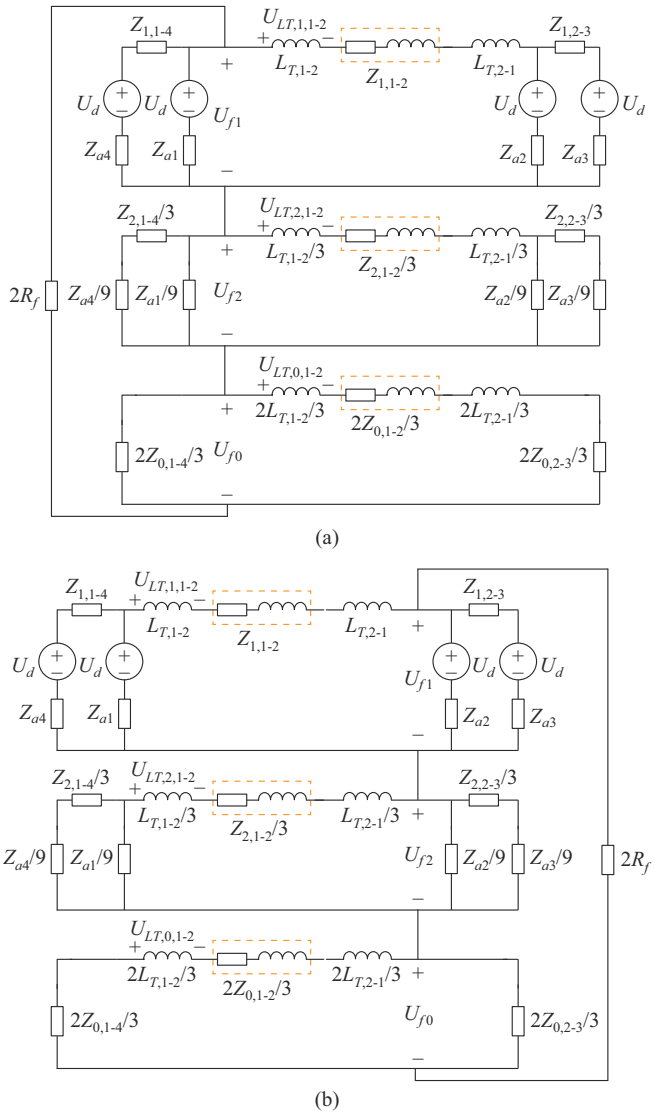

Fig. 6. Composite modulus circuits under different EFs. (a) BEF. (b) FEF.

III. Proposed Protection Method

A. Protection Initiation Principle

During the normal operation, the differential of the 1M voltage on the DC bus $\mathrm{d}U_{L1}/\mathrm{d}t$ is 0. When a DC fault occurs, the amplitude of $\mathrm{d}U_{L1}/\mathrm{d}t$ is much larger than 0, which is used as the protection initiation criterion, as shown by:

$$\left|\frac{\mathrm{d}U_{L1}}{\mathrm{d}t}\right| > p_{set} \tag{11}$$

The sampling rate is set to be 100 kHz and the protection is activated when $\left|\mathrm{d}U_{L1}/\mathrm{d}t\right|$ exceeds the threshold value p_{set}. In this study, p_{set} is set to be 0.5 kV/μs.

B. Fault Detection Method Based on Modal Voltage

The previous analysis of the 1M voltage of CLR reveals that $U_{LT,1,1-2}$ is negative when a BEF occurs and is positive when an IF or FEF occurs. Because of the boundary effect of CLR, the amplitude of $U_{LT,1,1-2}$ is greater under an IF than that under an FEF.

Through the methods described in [18] and [28], (4) can be simplified and the time-domain expression for $U_{LT,1,1-2}$ in the case of IFs can be derived as:

$$U_{LT,1,1-2}(t) = L_{T,1-2}\sqrt{\left(U_{dc0}-\frac{I_{dc0}R_{eq,IF}}{2}\right)^2\frac{1}{\omega^2 L_{eq,IF}^2}+I_{dc0}^2}\,\mathrm{e}^{-\alpha t}\cdot \left(-\alpha\sin(\omega t+\beta)+\omega\cos(\omega t+\beta)\right) \tag{12}$$

where U_{dc0} and I_{dc0} are the initial voltage of C_a and initial current of L_a, respectively. The remaining relevant parameters satisfy:

$$\begin{cases} \alpha = \dfrac{R_{eq,IF}}{2L_{eq,IF}} \\ \beta = \arctan\left(\dfrac{2I_{dc0}}{(2U_{dc0}-I_{dc0}R_{eq,IF})\omega L_{eq,IF}}\right) \\ \omega = \sqrt{\dfrac{1}{L_{eq,IF}C_a}-\dfrac{R_{eq,IF}^2}{4L_{eq,IF}^2}} \end{cases} \tag{13}$$

$$\begin{cases} L_{eq,IF} = \dfrac{6L_{0,1-4}+18L_{T,1-2}+10L_{a1}+6xL_{0,1-2}+9xL_{1,1-2}+3xL_{2,1-2}}{9} \\ R_{eq,IF} = \dfrac{6R_{0,1-4}+18R_{f1}+10R_{a1}+6xR_{0,1-2}+9xR_{1,1-2}+3xR_{2,1-2}}{9} \\ R_{f1} = \dfrac{Z_{tot}}{Z_1+\dfrac{1}{3}Z_{22}+\dfrac{2}{3}Z_{02}}2R_f \\ Z_{tot} = Z_1+Z_3+\dfrac{1}{3}(Z_{21}+Z_{22})+\dfrac{2}{3}(Z_{01}+Z_{02}) \end{cases} \tag{14}$$

As shown in Figs. 5(a) and 6(b), the main difference between the FEF and IF is the CLR on the DC line. Therefore, when an FEF occurs, the time-domain expression for $U_{LT,1,1-2}$ is similar to that when an IF occurs.

To reduce the noise effect, the transient mean value of CLR modal voltage $p(U_1)$ is used as the protection index, as expressed by:

$$p(U_1) = \frac{\int_0^{\Delta T} U_{LT,1,1-2}(\tau)\mathrm{d}\tau}{\Delta T} \tag{15}$$

where ΔT is a specific time period.

Using (12)-(15), we can calculate the value of $p(U_1)$ for the HIF ($R_f = 300\ \Omega$) at $x = 100\%$ and the solid FEFs. In this study, the protection threshold p_1 is set with the boundary for identifying the HIF ($R_f = 300\ \Omega$) at $x = 100\%$, where p_1 should be greater than the value of $p(U_1)$ for metallic FEFs to ensure the accuracy of protection. In this study, p_1 is 100 kV.

Based on the previous analysis of the 2M and 0M voltages of CLR, we can see that the polarities of the 2M and 0M voltages have different characteristics under different fault types, as listed in Table I.

TABLE I
POLARITIES OF 2M AND 0M VOLTAGES OF CLR

Fault	Polarity	
	2M voltage	0M voltage
PGF	+	+
NGF	−	−
PMF	+	0
NMF	−	0
PNF	0	0

As Table I shows, the polarity of the 0M voltage of CLR can distinguish between pole-to-ground faults, and the polarity of the 2M voltage of CLR can distinguish between PMF and pole-to-pole faults. Using the transient mean value of CLR modal voltage does not affect the polarity of the modal voltage and reduces the effect of noise. Therefore, the transient mean values of 2M and 0M voltages, i.e., $p(U_2)$ and $p(U_0)$, respectively, are used to identify the faulty poles. Taking $p(U_2)$ and $p(U_0)$ as the axes, the pole-selection phase plane is constructed, as shown in Fig. 7.

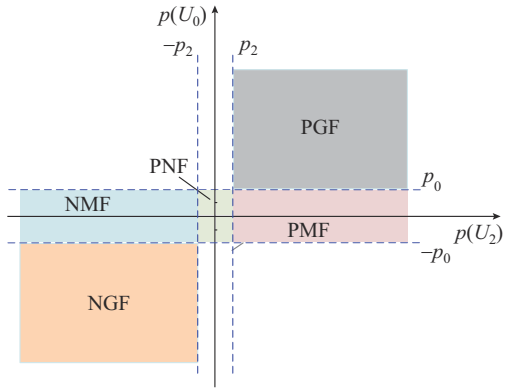

Fig. 7. Pole-selection phase plane based on $p(U_2)$ and $p(U_0)$.

As shown in Fig. 7, different fault types can be assigned to different regions of the phase plane, where p_2 and p_0 are the corresponding protection thresholds, which are ideally 0. However, in practical engineering, possible measurement errors and voltage levels should be considered. In this study, p_2 and p_0 are set to be 1.5 kV.

C. Adaptive Protection

The single-end protection method is prone to the boundary effect of CLR, which may lead to a misjudgment of IF and fail to operate when an HIF occurs at $x=100\%$. This study proposes a novel solution to address this problem by introducing a threshold scaling factor K_n based on the initial fault information, as defined in:

$$K_n=\begin{cases}\dfrac{K-K_{\min}}{0.5(K_{\max}-K_{\min})} & K\le 0.5(K_{\max}+K_{\min})\\ \dfrac{K_{\max}-K}{0.5(K_{\max}-K_{\min})} & K>0.5(K_{\max}+K_{\min})\end{cases} \tag{16}$$

where K is the peak value of the differential of 1M voltage on DC bus under a fault; and $K_{\max}$ and $K_{\min}$ are the maximum and minimum values of K under a solid fault at $x=0\%$ and an HIF ($R_f=300\ \Omega$) at $x=100\%$, respectively.

When a fault occurs, the value of K is collected and the corresponding value of K_n is calculated. The adaptive protection threshold $p_{1\text{-}1}$ is then calculated ($p_{1\text{-}1}=p_1K_n$). The more minor the fault is, the closer K is to $K_{\min}$. In addition, at this time, K_n and $p_{1\text{-}1}$ are smaller. As the adaptive protection threshold $p_{1\text{-}1}$ decreases, the HIF initially rejected by protection can be sensitively recognized. Similarly, the more severe the fault is, the closer K is to $K_{\max}$, and the smaller K_n and $p_{1\text{-}1}$ are. As the adaptive protection threshold $p_{1\text{-}1}$ decreases, the fault identification conditions are satisfied and the protection can be activated, both at a faster rate. To prevent an improper protection operation caused by very small values, this study sets the saturation value of the threshold scaling factor K_n to be 0.5.

D. Protection Process

Figure 8 illustrates the protection process based on the transient mean value of CLR modal voltage. First, the bus voltage and CLR voltage are obtained. The value of $\left|\mathrm{d}U_{L1}/\mathrm{d}t\right|$ is then calculated, and whether the protection is activated is determined. If the conditions for protection activation are satisfied, the corresponding CLR modal voltages and threshold scaling factor K_n are calculated. The adaptive protection threshold $p_{1\text{-}1}$ is then calculated, and the location of the fault is determined. The fault is recognized as an IF when $p(U_1)$ exceeds the adaptive protection threshold $p_{1\text{-}1}$. If the fault is then recognized as an IF, the corresponding fault pole is identified according to Table I and Fig. 7. Only the DCCBs on the fault lines are tripped. The protection signal is sent when the corresponding fault conditions are satisfied by eight sampling points.

IV. SIMULATION RESULTS

A multi-terminal DC grid with DMR is constructed on the PSCAD/EMTDC platform, as shown in Fig. 1. Table II lists the MMC parameters. The OHL is modeled using a frequency-dependent model, as shown in Supplementary Material A. The specific parameters of OHL are given as follows. The unit resistance and inductance on the OHL are $R=32$ mΩ/km and $L=1.8$ mH/km, respectively. The grounding and phase capacitors are 0.0078 and 0.0085 μF/km, respectively. The lengths of lines between MMCs are $l_{12}=219$ km, $l_{23}=66$ km, $l_{34}=227$ km, and $l_{41}=126$ km. The inductance of CLR is 0.15 H. The operating time of DCCB is 2 ms.

A. Fault Pole Selection

Figure 9(a) and (b) shows $p(U_2)$ and $p(U_0)$ under different IF types, respectively. Here, $x=80\%$, the fault transition resistance R_f is 50 Ω, and p_0 and p_2 are both set to be 1.5 kV.

The polarities $p(U_0)$ and $p(U_2)$ are different under different IF types: PGF and PMF have a positive polarity of $p(U_2)$, whereas NGF and NMF have a negative polarity of $p(U_2)$. In addition, under the PNF, $p(U_2)=0$. For $p(U_0)$, a positive polarity characterizes the PGF, whereas a negative polarity characterizes NGF. Under the PMF, NMF, and PNF, $p(U_0)=0$.

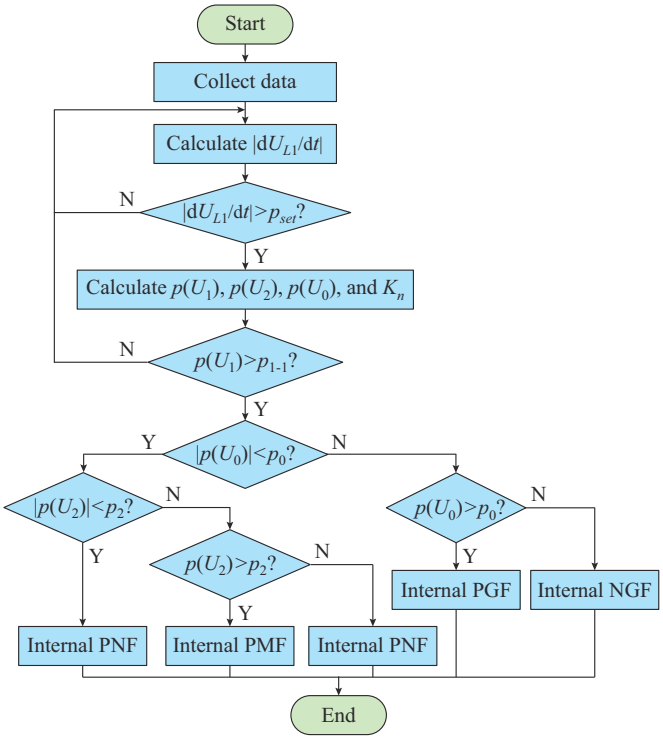

Fig. 8. Protection process based on transient mean value of CLR modal voltage.

Figure 10 illustrates the pole-selection phase plane for the IF. Different fault types are clearly distinguished by the boundaries.

B. Adaptive Protection Verification

The characteristics of U_{L1} and $p(U_1)$ are investigated when the PGF occurs at $x=10\%$ and $x=100\%$. As shown in Fig. 11(a) and (b), R_f varies from 0 to 300 Ω. With a solid fault at $x=10\%$, if a fixed threshold in the original protection method $p_1=100$ kV is used, eight sampling points are required to satisfy $p(U_1)>100$ kV. If a threshold scaling factor K_n is introduced, the adaptive protection threshold is reduced to $p_{1\text{-}1}$. Eight sampling points are only required to satisfy $p(U_1)>p_{1\text{-}1}$. The time required to satisfy the identification condition of IF is reduced, and the protection can be activated more quickly.

Figure 11(c) and (d) shows the variations in $|\mathrm{d}U_{L1}/\mathrm{d}t|$ and $p(U_1)$ for HIFs at $x=100\%$ with different R_f, respectively. When R_f is 500 Ω, the protection fails to operate with a fixed threshold. However, after the threshold scaling factor K_n is introduced, the adaptive protection threshold decreases to $p_{1\text{-}1}=50$ kV. Accordingly, there are sufficient sampling points to satisfy the fault identification condition, and the protection can operate successfully.

TABLE II
MMC PARAMETERS

MMC	Rated capacity (MW)	Rated DC voltage (kV)	Rated AC voltage (kV)	Transformer ratio	Leakage reactance (p.u.)	Bridge arm inductance (mH)	Submodule capacitance (mF)	Submodule number
MMC_1	1500	±500	500	525 kV/260 kV	0.15	88	7	233
MMC_2	1500	±500	500	230 kV/260 kV	0.15	44	7	233
MMC_3	3000	±500	220	230 kV/260 kV	0.15	44	15	233
MMC_4	3000	±500	220	525 kV/260 kV	0.15	88	15	233

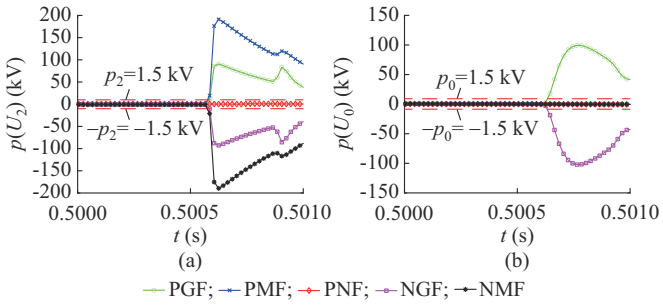

Fig. 9. $p(U_2)$ and $p(U_0)$ under different IF types. (a) $p(U_2)$. (b) $p(U_0)$.

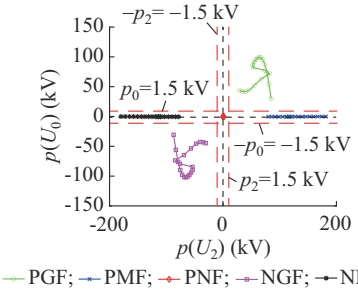

Fig. 10. Pole-selection phase plane for IF.

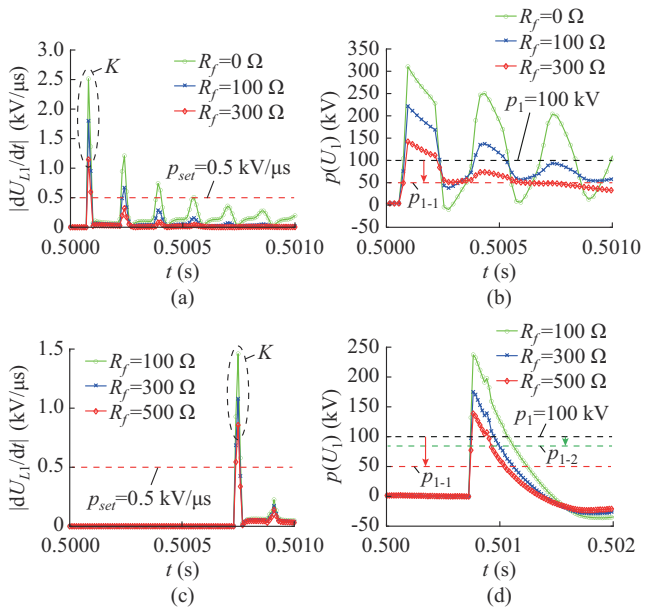

Fig. 11. Comparison of original and adaptive protection methods. (a) $|\mathrm{d}U_{L1}/\mathrm{d}t|$ when $x=10\%$. (b) $p(U_1)$ when $x=10\%$. (c) $|\mathrm{d}U_{L1}/\mathrm{d}t|$ when $x=100\%$. (d) $p(U_1)$ when $x=100\%$.

C. Other Pole-to-pole Faults

Various pole-to-pole faults exist, including PP-to-DMR-to-NP faults (PMNFs), PP-to-DMR-to-NP-to-ground faults (PMNGFs), and PNFs. To ensure that pole-to-pole faults can be accurately identified, two other pole-to-pole faults (PMNGF and PMNF) are investigated in this study.

Figure 12(a) and (b) shows pole and modal voltages, respectively, when a PMNGF ($x=50\%$, $R_f=0\ \Omega$) occurs in DC system. Both the 2M and 0M voltages are 0, so the pole-to-pole faults are identified. Figure 13(a) and (b) shows the pole and modal voltages, respectively, when a PMNF occurs ($x=50\%$, $R_f=0\ \Omega$), which is similar as that under a PMNGF or PNF. Therefore, the proposed protection method can identify pole-to-pole faults.

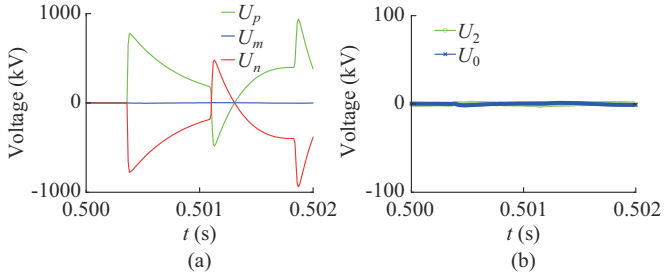

Fig. 12. Pole and modal voltages under PMNGF. (a) Pole voltage. (b) Modal voltage.

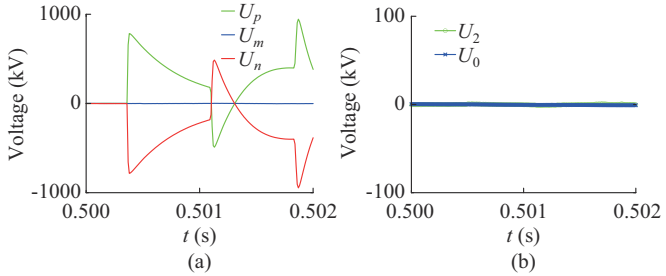

Fig. 13. Pole and modal voltages under PMNF. (a) Pole voltage. (b) Modal voltage.

D. Effects of Distributed Parameters

To analyze the effects of distributed parameters on protection, we change the line length L from 300 to 600 km. When a PGF occurs at the end of the line with $R_f=0.2\ \Omega$, the modal voltage changes, as shown in Fig. 14.

Despite the increase in line length, $|\mathrm{d}U_{L1}/\mathrm{d}t|$, $p(U_1)$, $p(U_2)$, and $p(U_0)$ all exceed their thresholds of p_{set}, p_1, p_2, and p_0, respectively. As Fig. 14 illustrates, the number of sampling points that conform to the PGF criteria decreases as the line length increases. In addition, the modal voltage changes at a later time as the line length increases. Therefore, the time required for the protection to recognize faults gradually increases from 1 to 2.5 ms. Even when the line length is increased to 600 km, the fault recognition conditions are still satisfied.

E. Effects of CLR

Figure 15 shows the modal voltages under different inductancecs of CLR when a PGF ($x=100\%$, $R_f=300\ \Omega$) occurs.

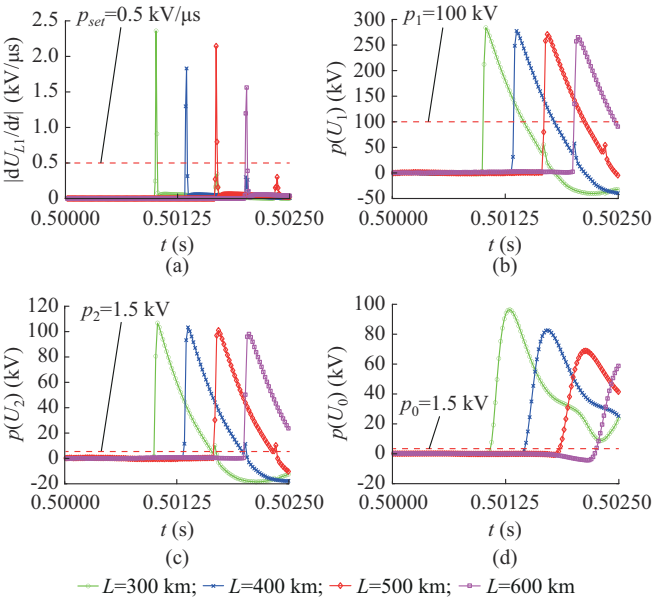

Fig. 14. Modal voltages with different line lengths. (a) $|\mathrm{d}U_{L1}/\mathrm{d}t|$. (b) $p(U_1)$. (c) $p(U_2)$. (d) $p(U_0)$.

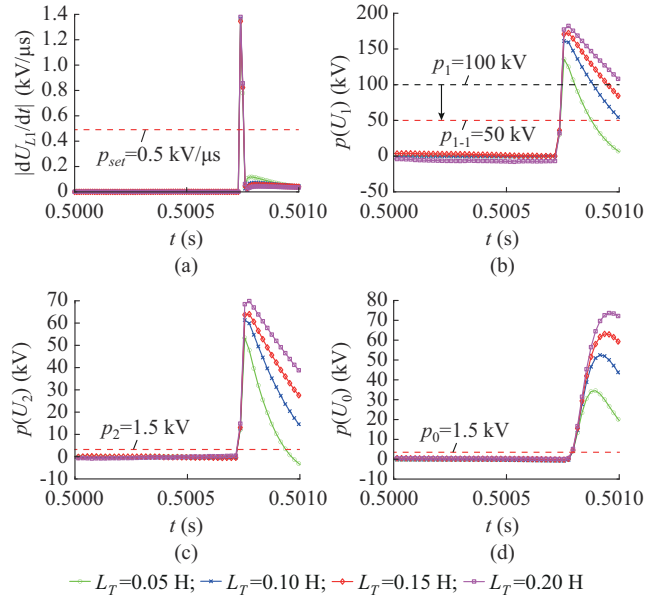

Fig. 15. Modal voltages under different inductances of CLRs. (a) $|\mathrm{d}U_{L1}/\mathrm{d}t|$. (b) $p(U_1)$. (c) $p(U_2)$. (d) $p(U_0)$.

As Fig. 15(a) illustrates, the change in the inductance of CLR has little effect on the change in the bus voltage and does not affect the protection activation. However, Fig. 15(b)-(d) shows that as the inductance of CLR decreases, the CLR modal voltages also decrease. When the inductance of CLR is 0.05 H, the fault can still be accurately recognized as an IF due to the adaptive protection threshold. In addition, there are sufficient sampling points satisfying $p(U_2)>p_2$ and $p(U_0)>p_0$. Thus, the protection can accurately identify the fault pole. Moreover, the inductance of CLR is usually greater than 0.05 H. Therefore, a change in the inductance of CLR does not cause the protection method to fail.

F. Effects of Sampled Noise

The proposed protection method is based on data analysis, so its effectiveness is sensitive to the sampled noise. The noise intensity is generally measured using the signal-to-noise ratio (SNR), where a small SNR indicates strong noise. This subsection investigates the effect of sampled noise on the protection with an SNR of 10 dB. The fault is set at $x=100\%$, the fault type is PGF, and $R_f=300\ \Omega$.

As shown in Fig. 16, the effects of sampled noise on the protection are negligible, and more than eight sampling points fall in the corresponding pole-selection phase plane within 1 ms. In the practical applications, multiple continuous noise-sampled points in the same fault area hardly happen, which ensures noise immunity of this method.

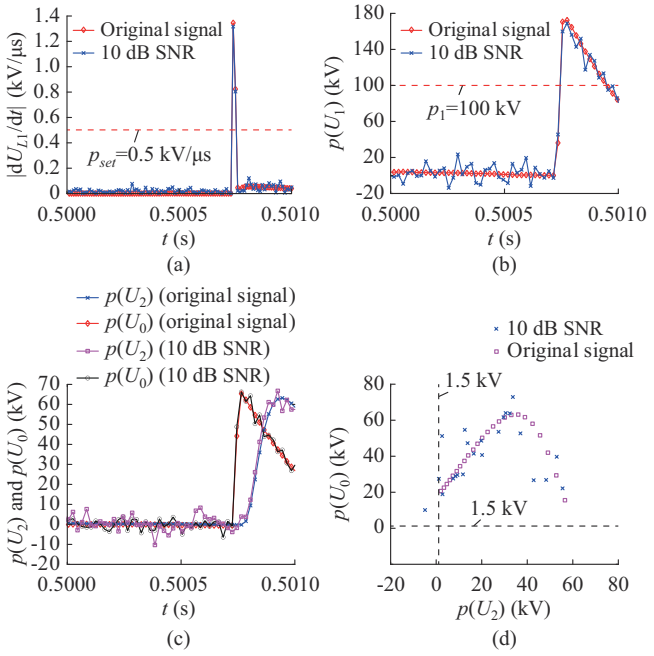

Fig. 16. Pole-selection phase plane under sampled noise. (a) $|dU_{L1}/dt|$. (b) $p(U_1)$. (c) $p(U_2)$ and $p(U_0)$. (d) Phase plane.

G. Comparison with Existing Methods

We compare the proposed protection method with existing methods in four respects: sampling frequency, ability to identify HIFs, noise immunity, and whether DMR is considered, as provided in Table III.

In [26], a protection method using the single-end rate of change of voltage is proposed for a DC grid with DMR. When different fault types occur at $x=80\%$ with $R_f=50\ \Omega$, the line modal voltage changes, as shown in Fig. 17. Figure 17(a) and (b) shows that the 0M voltages of PMF, NMF, and PNF are all unchanged. Therefore, it is not possible to effectively identify the corresponding fault poles.

In [32], a fault pole identification criterion is constructed using the 0M voltage. Figure 18 shows the 0M voltage when PGF, PNF, and PMF occur. The 0M voltage of PGF is less than 0, and that of PNF is equal to 0. When a PMF occurs, the 0M voltage is also equal to 0. Therefore, the protection method in [26] cannot distinguish between pole-to-pole and pole-to-DMR faults.

TABLE III
COMPARISON WITH EXISTING METHODS

Method	Sampling frequency (kHz)	R_f (Ω)	SNR (dB)	Is DMR considered?
Proposed	100	500	10	Yes
[20]	100	380		No
[22]	20	300	30	No
[23]	100	200	10	No
[26]	40	300	30	Yes
[29]	20	200	50	No
[30]	1000	300		No
[31]	200	500	40	No
[32]	500	500	30	No
[33]	100	500	25	No
[34]	100	300		No
[35]	50	200	35	No

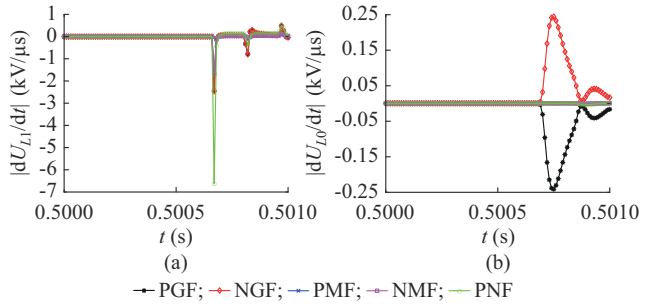

Fig. 17. Line modal voltage variation under different fault types. (a) $|dU_{L1}/dt|$. (b) $|dU_{L0}/dt|$.

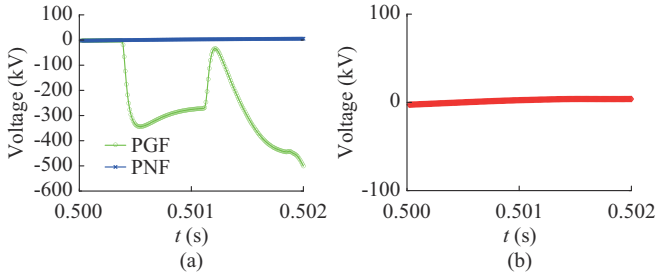

Fig. 18. 0M voltage under different fault types. (a) PGF and PNF. (b) PMF.

In [34], a fault identification criterion is constructed based on the difference in the line transient traveling wave (TW) power. Figure 19(a) and (b) shows the transient TW power under the PGF ($x=100\%$, $R_f=500\ \Omega$) and the solid FEF, respectively. The peak value of differential transient TW power is –210 MW when a PGF occurs. When a solid FEF occurs, the peak value of differential transient TW power is –470 MW. The power amplitude corresponding to FEF is greater than that corresponding to PGF. Accordingly, the protection method cannot effectively identify external faults.

H. Experiment

To demonstrate the applicability of the proposed protection method, we construct an experimental platform for a bipolar DC system with DMR based on the real-time simulation system, i.e., RT-LAB, as shown in Fig. 20.

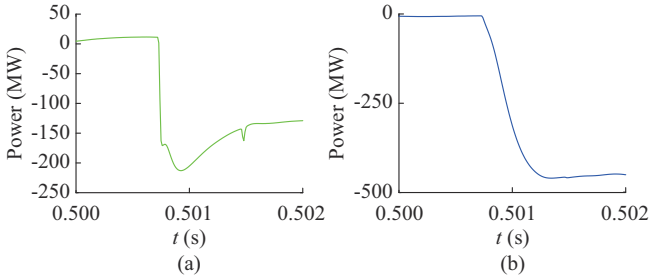

Fig. 19. Transient TW power under different fault types. (a) PGF. (b) Metallic FEF.

Fig. 20. Experimental platform based on RT-LAB.

The experimental platform can simulate controller characteristics through hardware-in-the-loop experiments and real samples by extracting measurement data from an oscilloscope. Table IV lists the parameters of the experimental platform, where U_{dc1} and U_{dc2} are the DC voltages at two ends of lines.

TABLE IV
PARAMETERS OF EXPERIMENTAL PLATFORM

Parameter	Value	Parameter	Value
U_{dc1} (kV)	100	C_a (mF)	1.2
U_{dc2} (kV)	100	L_T (mH)	1
L_a (mH)	10	R (Ω)	1
R_a (Ω)	0.01	L (mH)	40

Figure 21 shows the CLR pole voltages when different fault types occur at $x=0\%$ ($R_f=0$ Ω). The CLR modal voltages are obtained by calculating the collected data, as shown in Fig. 22. It can be observed that the 2M voltage can distinguish asymmetrical faults, whereas the 0M voltage can distinguish ground faults. Figure 23 shows the phase plane consisting of CLR modal voltages, where different fault types are classified into different regions. Therefore, this phase-plane based protection method can effectively identify fault poles.

Figure 24 shows the CLR pole voltages when an external fault ($R_f=0$ Ω) and an internal HIF ($R_f=100$ Ω) occur, and the fault type is PNF. The CLR modal voltages are obtained by calculating the collected data, as shown in Fig. 25. The two figures show that the amplitude of the 1M voltage can be used to distinguish between internal and external faults. The 2M and 0M voltages are approximately 0, and therefore the fault pole can be identified.

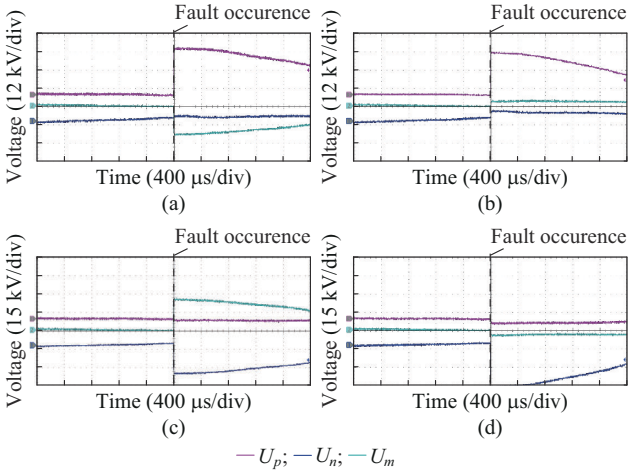

Fig. 21. Experimental results for CLR pole voltages under different fault types. (a) PMF. (b) PGF. (c) NMF. (d) NGF.

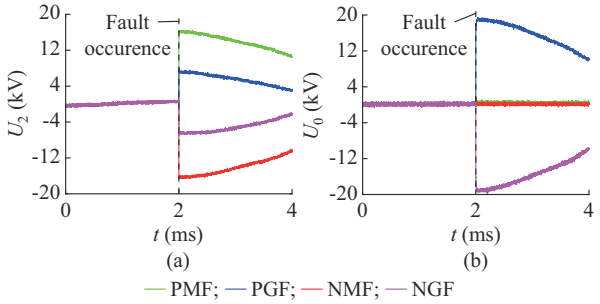

Fig. 22. CLR modal voltages under different fault types. (a) 2M voltage. (b) 0M voltage.

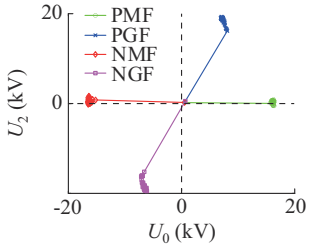

Fig. 23. Phase plane consisting of CLR modal voltages.

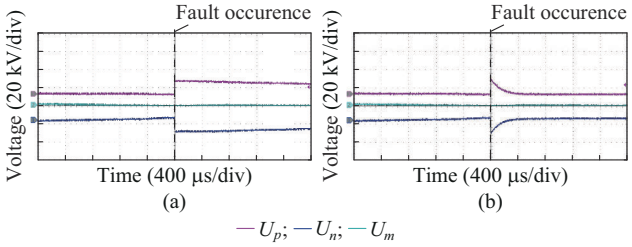

Fig. 24. Experimental results for CLR pole voltages at different fault positions. (a) External fault. (b) Internal HIF.

V. CONCLUSION

This study proposes a novel single-end protection method for DC grids with DMR based on the transient mean value of CLR modal voltage.

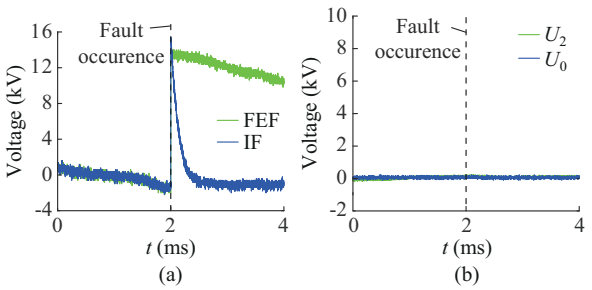

Fig. 25. CLR modal voltages at different fault positions. (a) 1M voltages. (b) 2M and 0M voltages.

The modulus circuits are developed for the MMC, DC transmission lines, and R_f. Integrated circuits are then determined to reveal the voltage characteristics of the CLR. The simulation and experimental results are summarized as follows.

1) The proposed protection method can accurately identify different fault types under the pole-selection phase plane, which is constructed by 2M and 0M voltages of CLR. The 1M voltage of CLR can effectively distinguish between internal and external faults, and the proposed protection method can reliably activate the protection.

2) A threshold scaling factor is proposed to improve the protection capabilities in identifying HIFs with a fault resistance of 500 Ω. In addition, the proposed protection method identifies faults within 1 ms and is immune to 10 dB of SNR.

3) The line length and the inductance value of CLR affect the performance of the proposed protection method in identifying faults. As the line length increases, the time required for protection to detect a fault increases. The ability to detect HIFs is weakened if the inductance of CLR is too low.

4) Compared with other single-end protection methods, the proposed protection method has robust noise immunity, outstanding fault pole identification capabilities, and proficiency in detecting HIFs.

REFERENCES

[1] J. A. Ansari, C. Liu, and S. A. Khan, "MMC based MTDC grids: a detailed review on issues and challenges for operation, control and protection schemes," *IEEE Access*, vol. 8, pp. 168154-168165, Sept. 2020.

[2] W. Xiang, S. Yang, G. P. Adam *et al*., "DC fault protection algorithms of MMC-HVDC grids: fault analysis, methodologies, experimental validations, and future trends," *IEEE Transactions on Power Electronics*, vol. 36, no. 10, pp. 11245-11264, Oct. 2021.

[3] Y. Li, L. Wu, J. Li *et al*., "DC fault detection in MTDC systems based on transient high frequency of current," *IEEE Transactions on Power Delivery*, vol. 34, no. 3, pp. 950-962, Jun. 2019.

[4] C. W. Gellings, "A globe spanning super grid," *IEEE Spectrum*, vol. 52, no. 8, pp. 48-54, Aug. 2015.

[5] W. Xiang, S. Yang, L. Xu *et al*., "A transient voltage-based DC fault line protection scheme for MMC-based DC grid embedding DC breakers," *IEEE Transactions on Power Delivery*, vol. 34, no. 1, pp. 334-345, Feb. 2019.

[6] Y. Guo, Q. Xu, and R. Han, "DC short faults and fault current limiting technologies in flexible DC grid: a review," in *Proceedings of 2019 IEEE PES Asia-Pacific Power and Energy Engineering Conference*, Macao, China, Dec. 2019, pp. 1-6.

[7] W. Xiang, H. Zhang, S. Yang *et al*., "A differential pilot protection scheme for MMC-based DC grid resilient to communication failure," *IEEE Journal of Emerging and Selected Topics in Power Electronics*, vol. 9, no. 5, pp. 5631-5645, Oct. 2021.

[8] M. Farshad, "A pilot protection scheme for transmission lines of half-bridge MMC-HVDC grids using cosine distance criterion," *IEEE Transactions on Power Delivery*, vol. 36, no. 2, pp. 1089-1096, Apr. 2021.

[9] B. Li, Y. Li, and J. He, "A DC fault handling method of the MMC-based DC system," *International Journal of Electrical Power & Energy Systems*, vol. 93, pp. 39-50, Dec. 2017.

[10] S. Zhang, G. Zou, Q. Huang *et al*., "Single-ended line protection for MMC-MTDC grids," *IET Generation, Transmission & Distribution*, vol. 13, no. 19, pp. 4331-4338, Oct. 2019.

[11] T. Lan, Y. Li, and X. Duan, "High fault-resistance tolerable traveling wave protection for multi-terminal VSC-HVDC," *IEEE Transactions on Power Delivery*, vol. 36, no. 2, pp. 943-956, Apr. 2021.

[12] D. Li, A. Ukil, K. Satpathi *et al*., "Improved S transform-based fault detection method in voltage source converter interfaced DC system," *IEEE Transactions on Industrial Electronics*, vol. 68, no. 6, pp. 5024-5035, Jun. 2021.

[13] L. Sabug Jr, A. Musa, F. Costa *et al*., "Real-time boundary wavelet transform-based DC fault protection system for MTDC grids," *International Journal of Electrical Power & Energy Systems*, vol. 115, p. 105475, Feb. 2020.

[14] W. Xiang, S. Yang, and J. Wen, "ANN-based robust DC fault protection algorithm for MMC high-voltage direct current grids," *IET Renewable Power Generation*, vol. 14, no. 2, pp. 199-210, Feb. 2020.

[15] R. Muzzammel and A. Raza, "Low impedance fault identification and classification based on Boltzmann machine learning for HVDC transmission systems," *Journal of Modern Power Systems and Clean Energy*, vol. 10, no. 2, pp. 440-449, Mar. 2022.

[16] P. Verrax, A. Bertinato, M. Kieffer *et al*., "Transient-based fault identification algorithm using parametric models for meshed HVDC grids," *Electric Power Systems Research*, vol. 185, p. 106387, Aug. 2020.

[17] P. Verrax, A. Bertinato, M. Kieffer *et al*., "Fast fault identification in bipolar HVDC grids: a fault parameter estimation approach," *IEEE Transactions on Power Delivery*, vol. 37, no. 1, pp. 258-267, Feb. 2022.

[18] Y. Li, J. Li, L. Xiong *et al*., "DC fault detection in meshed MTdc systems based on transient average value of current," *IEEE Transactions on Industrial Electronics*, vol. 67, no. 3, pp. 1932-1943, Mar. 2020.

[19] J. Li, Y. Li, L. Xiong *et al*., "DC fault analysis and transient average current based fault detection for radial MTDC system," *IEEE Transactions on Power Delivery*, vol. 35, no. 3, pp. 1310-1320, Jun. 2020.

[20] C. Li, A. M. Gole, and C. Zhao, "A fast DC fault detection method using DC reactor voltages in HVdc grids," *IEEE Transactions on Power Delivery*, vol. 33, no. 5, pp. 2254-2264, Oct. 2018.

[21] J. Sun, S. Debnath, M. Bloch *et al*., "A hybrid DC fault primary protection algorithm for multi-terminal HVDC systems," *IEEE Transactions on Power Delivery*, vol. 37, no. 2, pp. 1285-1294, Apr. 2022.

[22] J. Liao, N. Zhou, and Q. Wang, "DC grid protection method based on phase planes of single-end common- and differential-mode components," *IEEE Transactions on Power Delivery*, vol. 36, no. 1, pp. 299-310, Feb. 2021.

[23] S. Yang, W. Xiang, R. Li *et al*., "An improved DC fault protection algorithm for MMC HVDC grids based on modal-domain analysis," *IEEE Journal of Emerging and Selected Topics in Power Electronics*, vol. 8, no. 4, pp. 4086-4099, Dec. 2020.

[24] V. Nougain, S. Mishra, G. S. Misyris *et al*., "Multiterminal DC fault identification for MMC-HVDC systems based on modal analysis – a localized protection scheme," *IEEE Journal of Emerging and Selected Topics in Power Electronics*, vol. 9, no. 6, pp. 6650-6661, Dec. 2021.

[25] N. H. van der Blij, L. M. Ramirez-Elizondo, M. T. J. Spaan *et al*., "Symmetrical component decomposition of DC distribution systems," *IEEE Transactions on Power Systems*, vol. 33, no. 3, pp. 2733-2741, May 2018.

[26] W. Sima, Z. Fu, M. Yang *et al*., "Hybrid ROCOV/waveform similarity coefficient based protection for DC line in HVDC grids," *CSEE Journal of Power and Energy Systems*, doi: 10.17775/CSEEJPES.2020.06730

[27] S. Xue, J. Lu, Y. Sun *et al*., "A reverse travelling wave differential protection scheme for DC lines in MMC-HVDC system with metallic return," *International Journal of Electrical Power & Energy Systems*, vol. 135, p. 107521, Feb. 2022.

[28] H. Ye, S. Gao, G. Li *et al*., "Efficient estimation and characteristic analysis of short-circuit currents for MMC-MTDC grids," *IEEE Transactions on Industrial Electronics*, vol. 68, no. 1, pp. 258-269, Jan. 2021.

[29] M. J. Perez-Molina, D. M. Larruskain, P. Eguia *et al*., "Local derivative-based fault detection for HVDC grids," *IEEE Transactions on In-*

dustry Applications, vol. 58, no. 2, pp. 1521-1530, Mar. 2022.
[30] L. Tang, X. Dong, S. Shi *et al*., "A high-speed protection scheme for the DC transmission line of a MMC-HVDC grid," *Electric Power Systems Research*, vol. 168, pp. 81-91, Mar. 2019.
[31] C. Zhang, G. Song, A. P. S. Meliopoulos *et al*., "Setting-less nonunit protection method for DC line faults in VSC-MTdc systems," *IEEE Transactions on Industrial Electronics*, vol. 69, no. 1, pp. 495-505, Jan. 2022.
[32] D. Mu, S. Lin, P. He *et al*., "An improved method of traveling wave protection for DC lines based on the compensation of line-mode fault voltage," *IEEE Transactions on Power Delivery*, vol. 38, no. 3, pp. 1720-1730, Jun. 2023.
[33] L. Liu, A. Lekić, and M. Popov, "Robust traveling wave-based protection scheme for multiterminal DC grids," *IEEE Transactions on Power Delivery*, vol. 38, no. 5, pp. 3117-3129, Oct. 2023.
[34] F. Dai, Z. Zhou, and X. Wang, "Single-end protection scheme based on transient power waveshape for hybrid HVDC transmission lines," *Journal of Modern Power Systems and Clean Energy*, vol. 11, no. 5, pp. 1673-1686, Sept. 2023.
[35] M. Banafer and S. R. Mohanty, "Traveling wave-based primary protection and fault localization scheme for MTDC grid considering IEC 61869-9 measurement standard," *IEEE Transactions on Instrumentation and Measurement*, vol. 72, p. 9002116, May 2023.

Yuhong Wang received the B.S. and M.S. degrees in power system and its automation from Chongqing University, Chongqing, China, in 1993 and 1995, respectively, and the Ph.D. degree in power system and its automation from Southwest Jiaotong University, Chengdu, China, in 2008. She is currently a Professor with Sichuan University, Chengdu, China. Her research interests include power system stability and control, high voltage DC transmission (HVDC) and flexible AC transmission (FACT) systems, renewable energy integration, and artificial intelligence.

Zipen Tan received the B.E. degree in the College of Electrical Engineering from Sichuan University, Chengdu, China, in 2022, where he is currently pursuing the M.S. degree. His research interests include power system protection and control, and fault analysis and protection of DC grid.

Jianquan Liao received the B.S. degree in electrical engineering from the China University of Petroleum, Qingdao, China, in 2017, and the Ph.D. degree from Chongqing University, Chongqing, China, in 2021. From September 2019 to September 2020, he was a Guest Researcher of the Delft University of Technology, Delft, The Netherlands. He was with DC Systems, Energy Conversion and Storage Group in Electrical Sustainable Energy, Delft. He has been an Associate Research Fellow with the School of Electrical Engineering, Sichuan University, Chengdu, China, since 2021. His current research interests include power system protection and control, power quality of the DC distribution network, and power system stability and control.

Yangtao Liu received the B.S degree in mechanical and transportation engineering from China University of Petroleum, Beijing, China, in 2022. He is currently pursuing the M.S. degree at Sichuan University, Chengdu, China. His research interests include power system protection and control, and fault analysis and protection of DC grid.

Chunsheng Guo received the B.E. degree in the College of Electrical Engineering from Sichuan University, Chengdu, China, in 2017, and the M.Eng. degree in the Department of Electrical and Electronic Engineering from the University of Nottingham, Nottingham, UK, in 2018. He is currently pursuing the Ph.D. degree at Sichuan University. His research interests include power system protection and control, HVDC transmission, and voltage balancer.

Niancheng Zhou received the B.S., M.S., and Ph.D. degrees in electrical engineering from Chongqing University, Chongqing, China, in 1991, 1994, and 1997, respectively. He worked at Chongqing Kuayue Technology Co., Ltd., Chongqing, China, from 1997 to 2003. From 2010 to 2011, he was a Research Fellow of Nanyang Technological University, Singapore. He is currently a Professor in School of Electrical Engineering, Chongqing University. His research interests include analysis, operation of power system, microgrid, and power quality.

Qianggang Wang received the B.S. and Ph.D. degrees from Chongqing University, Chongqing, China, in 2009 and 2015, respectively. He is currently an Associate Professor with the School of Electrical Engineering in Chongqing University. He was a Research Fellow with Nanyang Technological University, Singapore, from 2015 to 2016. His research interests include analysis and operation of power systems, microgrid, and power quality.